Seismic Performance and Calculation Method of Precast Reduced Beam Section Connection

Hao Qi [1], Shaowei Hu [2,*], Xiang Xue [1], Changxi Shan [1], Wenhao Li [1], Yajia Wang [1] and Peiyi Wang [3]

[1] School of Civil Engineering, Chongqing University, Chongqing 400045, China; qihaocqu@outlook.com (H.Q.)
[2] Yellow River Laboratory, Zhengzhou University, Zhengzhou 450001, China
[3] China Construction Fifth Engineering Division Co., Ltd., Changsha 410004, China
* Correspondence: hushaowei@zzu.edu.cn

Abstract: To prevent brittle damage and improve the post-earthquake rapid repair capability of beam-column connections, a precast reduced beam section (PRBS) connection joint that can be rapidly repaired under earthquake action was proposed in this study. Four specimens, including a repaired specimen, were subjected to a quasi-static test to investigate the seismic performance and repair ability of the connection. Seismic performance indices such as the failure mode, hysteresis curve, skeleton curve, strain distribution, and ductility were obtained through observations and analyses. The results indicated that the novel connection exhibited superior load-bearing, energy dissipation, and rotation capacities, compared to the welded flange-bolted web and traditional bone-weakened connections. This novel connection effectively relocated the plastic hinge to alter the failure mode and prevent brittle damage. Additionally, rapid post-earthquake repair was achieved by replacing the dog-bone-style splice section, maintaining a high load-bearing capacity and seismic performance. Finite element (FE) models were established to analyze the mechanical behavior of the specimens, and a parametric analysis was conducted to study the influence of different parameters on the load-bearing capacity of the connection. Based on the experimental and FE analysis results, the possible yield and failure modes of the connection were analyzed, and a calculation method for the bearing capacity of the PRBS connection was proposed. A comparative result demonstrates that the proposed calculation method can accurately predict the load-carrying capacity of a connection.

Keywords: precast reduced beam section connection; earthquake resilient; dog-bone-style weakening; relocation of the plastic hinge; seismic rehabilitation

1. Introduction

The traditional beam-column connection mainly includes two forms: welded flange-bolted web and full-section welding connections, which are prone to brittle failure under earthquake action, leading to the failure and collapse of building structures [1–4]. The plastic hinge of the beam can be effectively transferred away from the connection surface of the beam and column through structural measures such as bone weakening of the flange, web opening, and web slotting [5–10]. The plastic hinge transfer method can significantly improve the energy dissipation capacity and ductility of a joint. However, it causes a large deformation at the plastic hinge after an earthquake, which leads to difficulties in realizing post-earthquake reinforcement and repair of the structure. Recently, assembled joints have been widely promoted because of their modular production and rapid construction [11–13]. Therefore, it is important to investigate the seismic performance of the assembled beam-column joints and their rapid repair capability after an earthquake.

Considerable research has been conducted on structural damage control and rapid repair performance of connections after an earthquake. Oh et al. [14] proposed a damper with a long and narrow hole for beam-column connections. The existence of the damper not only resulted in good seismic performance of the joints but also made the connection

easy to repair after the earthquake. Reza et al. [15] proposed a rubber–steel core damper for beam-to-column connections, where the combination of core steel and rubber improved the post-earthquake repairability of the connection. Huang et al. [16] conducted rapid repairs of a frame structure that had been damaged by an earthquake, and their study showed that the reinforced structure still exhibited good seismic performance. Ma et al. [17] proposed an artificial energy-dissipation plastic hinge and conducted an experimental study, which showed that the proposed plastic hinge can effectively control the plastic damage location and concentrate the energy dissipation at the plastic hinge. Ye et al. [18] proposed a type of assembled connection with a recoverable function, and their results indicated that the damage and failure of the connections were concentrated in the replaceable energy-dissipation hinge. Zhang et al. [19,20] proposed a series of splicing connections made with a cantilever beam that were subjected to pseudo-static loading. The results indicated that the main components of the connection could not be destroyed by a reasonable design. Zhang et al. [21] proposed a high-strength steel framed-tube structure with replaceable link beams and performed low-cycle reciprocating loading tests on its substructures, showing that the damage under the action of an earthquake was concentrated in the energy-dissipation beam section, and the remaining main components were in the elastic phase. In recent years, Özkılıç et al. [22–30] proposed various innovative connections to address the challenging issue of post-earthquake structural repair. An extensive series of experiments, FE analysis, and theoretical investigations were developed to study the load-bearing mechanisms of these novel connections. The results indicated that these novel connections exhibited favorable seismic performance and repairability characteristics.

Most studies on post-earthquake repair methods are complex. Therefore, a novel prefabricated reduced beam section (PRBS) connection joint with a bone-weakened beam section is proposed based on the concept of controllable damage and rapid repair following an earthquake. As shown in Figure 1, the key components of the PRBS connection joint include precast concrete-filled square steel tubular (CFST) columns with a cantilever short beam, a dog-bone-style splice section, and an H-beam. To ensure the structural strength of the connection between the short beam and the CFST column, and to mitigate the risk of brittle failure, the application of a bolted web-welded flange connection, as recommended in the specification [31], was employed. Each component was manufactured in a prefabrication plant and efficiently assembled at the construction site using web-connecting plates and frictional high-strength bolts. During seismic events, a plastic hinge of the connection is formed in the dog-bone-weakened beam section, and the structure can be restored for reuse by replacing the dog-bone-style splice section.
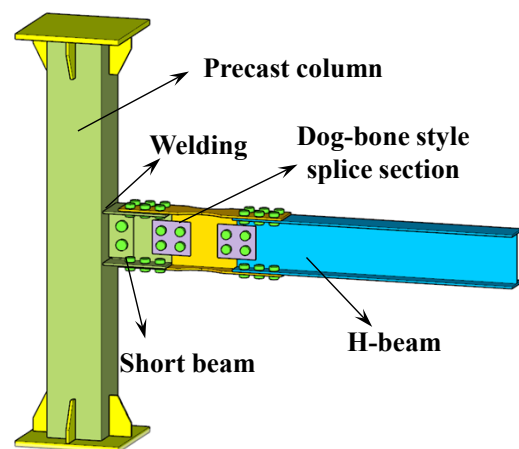

Figure 1. Proposed PRBS connection.

To investigate the seismic performance of the PRBS connection, quasi-static tests were conducted on welded flange-bolted web connection, a conventional bone-weakened, and a PRBS connection joints. A comparative analysis was performed on the failure

modes, hysteresis curves, strain distributions, and energy consumption of different joints. Additionally, the repaired PRBS connection joint was subjected to a quasi-static test to explore the seismic performance of the PRBS connection after repair. Furthermore, FE models were established to analyze the mechanical behavior of the specimens, and a parametric analysis was conducted to study the influence of different parameters on the load-bearing capacity of the connection. Ultimately, a load-carrying capacity calculation method for the PRBS connection was proposed based on experimental and FE results. These findings contribute to the theoretical foundation for the widespread adoption of this novel connection.

2. Experimental Program

2.1. Test Specimens

Four composite structural frame joint specimens were designed and fabricated in this study: a bolted web-welded flange joint, a traditional bone-weakened joint, a PRBS connection joint, and a repaired PRBS connection joint, named BASE, RBS, PRBS, and PRBS-R, respectively. The geometric dimensions of the PRBS-R specimen are the same as those of the PRBS specimen. The BASE specimen was a bolted web-welded flange joint designed according to the Chinese code [31]. The precast column was a CFST column with a cross-sectional size and the height of the square steel tube was 200 mm × 200 mm × 10 mm (length, width, and thickness) and 1500 mm, respectively. The cross-sectional size and length of the H-beam were 200 mm × 120 mm × 8 mm × 6 mm (height, width, flange thickness, and web thickness) and 1500 mm, respectively. The RBS specimen was designed based on the BASE specimen, and the dog-bone-weakening dimensions of the flange were determined according to the specifications [31]. The circular weakening length and depth were 160 and 25 mm, respectively.

Additionally, the PRBS specimen applied a dog-bone-weakening configuration to the splice section. The column size of the PRBS was identical to that of the BASE specimen. In accordance with AISC 358 [32], for the purpose of mitigating the failure risk associated with beam-column welding and adhering to the "strong column weak beam" design principle, it is imperative that the probable maximum moment at the face of the column (M_f) remains below the plastic moment of the beam, determined by the expected yield stress (M_{pe}) as illustrated in Equation (1) and Figure 2.

$$M_f \leq \varnothing M_{pe} \tag{1}$$

where $\varnothing$ is the resistance factor for ductile limit states, the recommended value for this parameter is 1 in this study. M_f and M_{pe} can be calculated using Equations (2)–(4).

$$M_f = M_{pd} L / L_1 \tag{2}$$

$$M_{pd} = C_{pr} R_y W_u f_y \tag{3}$$

$$M_{pe} = R_y W_u^b f_y \tag{4}$$

where M_{pd} is the probable maximum moment at the bone-weakening section; C_{pr} is the factor accounting for peak connection strength, the recommended value for this parameter is 1.1; W_u is the plastic section modulus for the bone-weakening section; W_u^b is the plastic section modulus for the full section of the beam at the face of the column, and R_y is the ratio of expected yield stress to specified minimum yield stress.

In addition, the splice between the dog-bone-style splice section and beam was designed using the principle of equal strength [33]; that is, the high-strength bolts on each side of the flange must endure the tensile load-bearing capacity of the flange, and the high-strength bolts on each side of the web must endure the shear load-bearing capacity of the web. Based on the above design requirements, the cross-sectional size and length of the H-

beam of the PRBS specimen were 200 mm × 120 mm × 8 mm × 6 mm (height, width, flange thickness, and web thickness) and 1030 mm, respectively. In addition, the dimensions of the flange and web plates of the dog-bone-style splice section were 600 mm × 120 mm × 8 mm (length, width, and thickness) and 70 mm × 200 mm × 6 mm (length, height, and thickness), respectively. The dimensions of the weakened area were identical to those of the RBS specimen. To ensure that the plastic hinge was concentrated in the splice section, the width of the short beam flange was increased to 160 mm. The cross-sectional size and length of the short beam were 200 mm × 160 mm × 8 mm × 6 mm (height, width, flange thickness, and web thickness) and 230 mm, respectively. The column, beam, and splice sections of the PRBS specimen satisfied the dimension limitations stipulated in the Chinese code [31]. Friction-type high-strength bolts of grade 10.9 s were used to connect various components of the joint; the bolt type at the web of the beam-column connection was M20 and the bolt type used in the other splicing parts was M16. The PRBS-R specimens were obtained by replacing the dog-bone-style splice sections of the PRBS specimens after the first test. There was no obvious plastic deformation in the flange and web bolt holes of the cantilever beam after the test of the PRBS specimen, which created construction conditions for replacing the dog-bone style splice section for the new fabricated connection. The geometric dimensions of the specimens are shown in Figure 3.
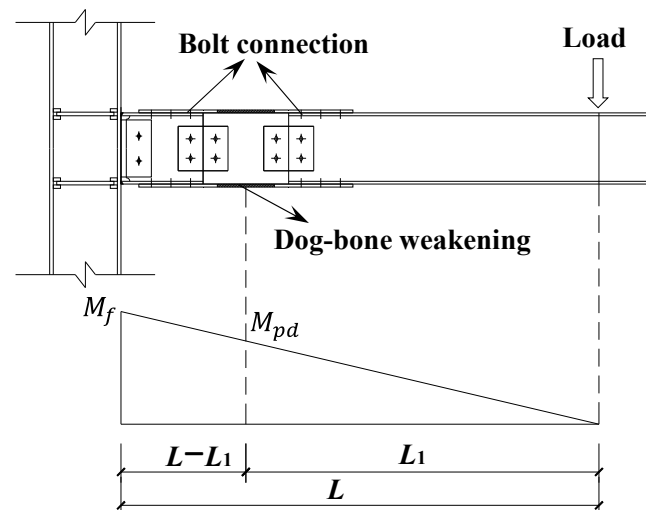

Figure 2. The gradient of the bending moment in PRBS connection.

2.2. Materials

A square steel tube was filled with C50 concrete. The compressive strength of the concrete cubes was tested according to the specifications stated in ref. [34] using 150 mm × 150 mm × 150 mm cube specimens. Three test cubes were examined, and the average cube compressive strength was 64.45 MPa.

Additionally, the steel grade of all the specimens was Q235 [31]. Tensile tests were performed on each type of steel plate according to the relevant material performance test specifications [35,36]. Three specimens were sampled and processed for each type of steel plate. The test results are presented in Table 1. In the table, the ultimate strain indicates the strain value corresponding to the maximum stress.

Table 1. Material properties of steel components.

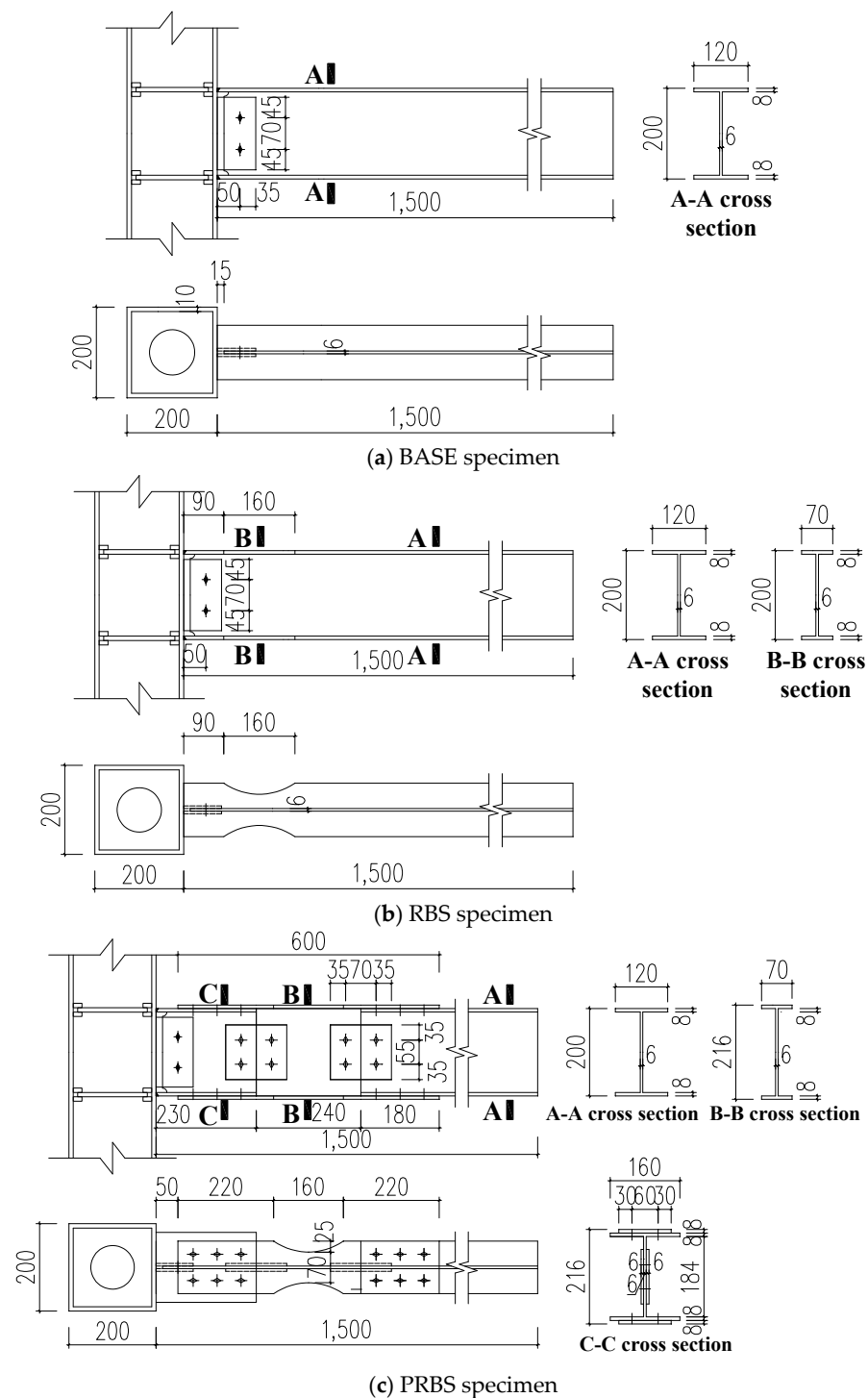| Member	Coupon Location	Thickness t (mm)	Yield Strength f_y (MPa)	Ultimate Strength f_u (MPa)	Young's Modulus E_s (MPa)	Ultimate Strain ε_u
Column	Square steel tube	10	303.3	448.3	202,115.0	0.178
Beam	Flange	8	281.7	435.0	201,738.0	0.185
	Web	6	348.3	513.3	216,503.7	0.152

(**a**) BASE specimen

(**b**) RBS specimen

(**c**) PRBS specimen

Figure 3. Dimensions of test specimens (Unit: mm).

2.3. Loading Device and Measurement Scheme

To accurately simulate the actual stress of the joint, the specimens were placed vertically and loaded onto the beam end. The loading device was composed of a self-balancing counterforce frame, electro-hydraulic servo actuator, lateral bracing, and horizontal bracing. The upper and lower ends of the column were connected to the actuator and the bottom beam of the counterforce frame, respectively, through the hinged device, and a 300 kN axial force was applied to the top of the column through the actuator considering the bearing capacity of the counterforce frame to simulate the actual upper load on the column. The beam end was connected to the actuator through a hinged device that applied cyclic

loading to the beam end. The horizontal displacement of the column top was limited by the horizontal bracing to ensure that the boundary condition of the column top was hinged. Lateral bracing limited the out-of-plane displacement of the beam to prevent out-of-plane instability during testing. The loading device used in the test is illustrated in Figure 4.
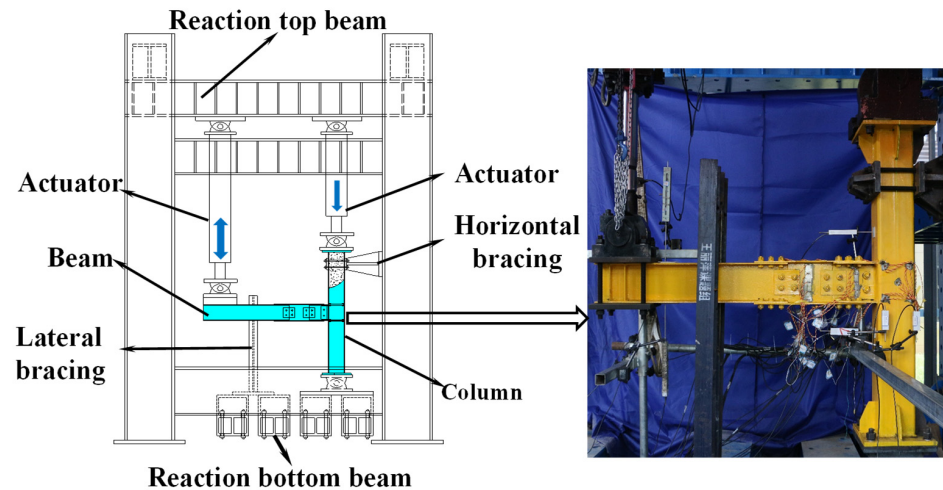

Figure 4. Loading device used in the test.

The test loading procedure adopted low-cycle reciprocating displacement-loading methods [33]. Each level of loading contained two cycles, and the inter-story drift angles of each level were 0.375%, 0.5%, 0.75%, 1%, 1.5%, 2%, 3%, 4%... In addition, the test was stopped when the load dropped to 85% of the peak load or the specimen was damaged. The specific inter-story drift angle and displacement amplitude are shown in Figure 5.

The displacement, load, and strain were measured in real time during the tests. The displacement of the load point in the beam was measured using the displacement sensor of the actuator, and the loads at the column top and beam end were measured using the force sensor of the force actuator. To accurately capture the stress distribution, time of the plastic hinge, plastic hinge distribution, and plastic development of the specimens during the experimental process, strain gauges were arranged at the corresponding positions of the square-steel tubular web, beam flange plate, and beam web plate. Because of the local damage to the repaired beam-column joint specimens, the residual strain caused by local plasticity affected the accuracy of the measurement results, and only the force and displacement data of the PRBS-R specimen were measured, not the strain data. The strain measurement scheme for the specimens is illustrated in Figure 6.
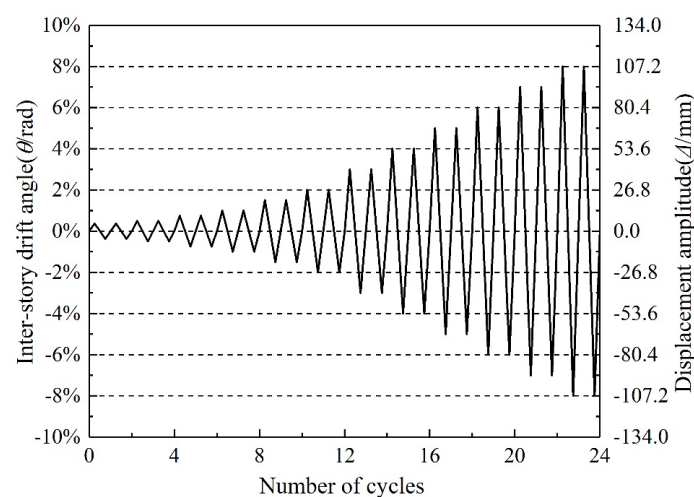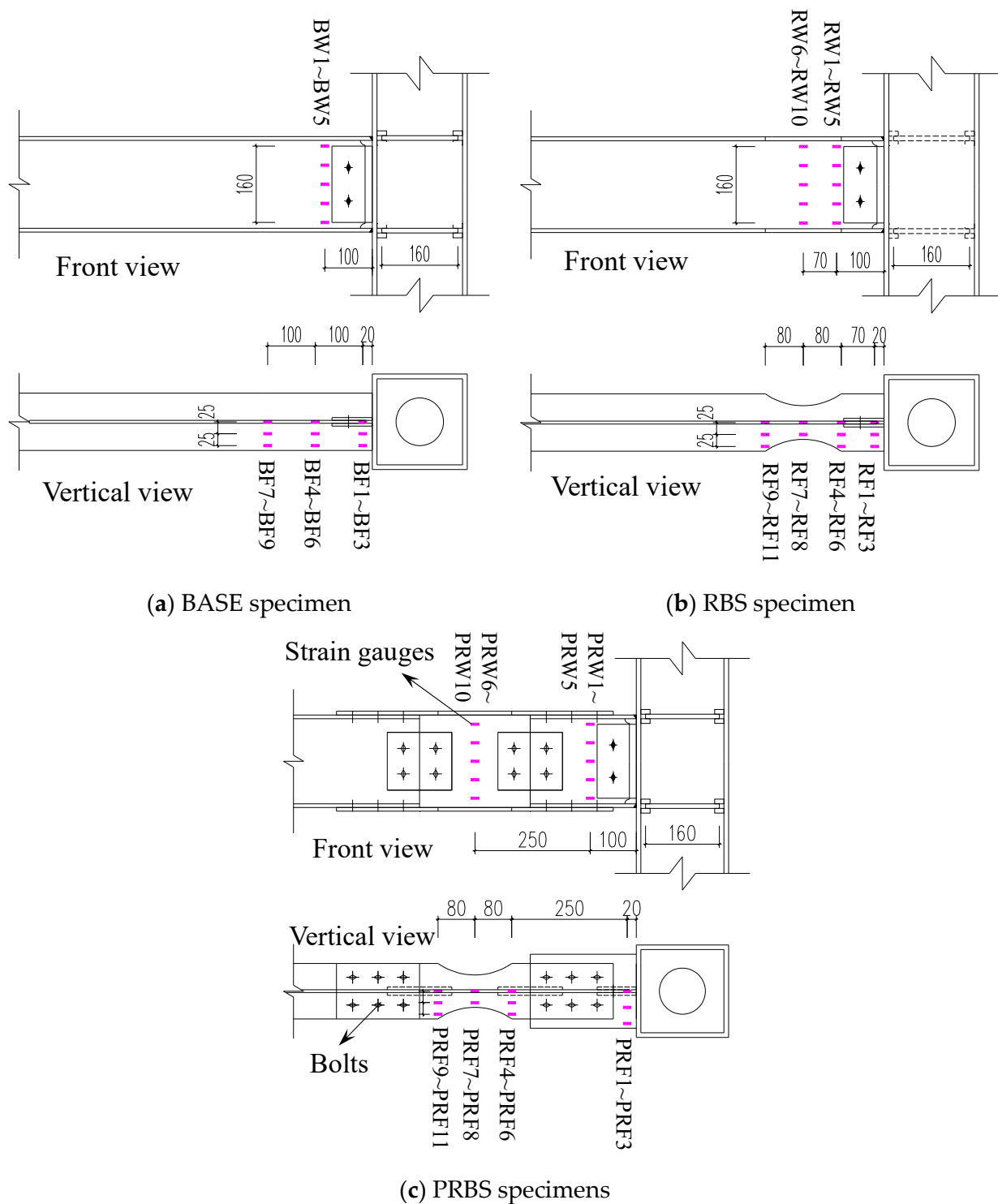

Figure 5. Loading procedure.

(**a**) BASE specimen

(**b**) RBS specimen

(**c**) PRBS specimens

Figure 6. Strain measurement scheme.

3. Test Phenomena and Failure Modes

3.1. BASE Specimen

In the early stage of the test, the hysteresis curve of the BASE specimen was linear, and the specimen was in the elastic stage with no evident phenomena. By increasing the loading cycle at the 1st cycle of the 1.5% story drift (Δ = −20.1 mm), the upper flange area near the column side of the steel beam began to show slight paint wrinkles due to compression, and the wrinkles flattened as the loading direction changed. At the first cycle of the 3%

story drift (Δ = −40.2 mm), local buckling occurred in the lower flange area of the steel beam near the column owing to compression, which was not fully recovered as the loading direction changed; this implies the generation of residual deformation. At the first cycle of the 4%-story drift (Δ = +53.6 mm), local buckling occurred in the roots of both upper and lower flanges, meanwhile, the slippage occurred in the high-strength bolt-connection area near the column side. As the displacement of the loading point reached the 2nd cycle of the 4% story drift (Δ = +53.6 mm), there was a non-penetrating crack in the middle of the upper flange near the side of the column, and the load-displacement curve showed that the bearing capacity decreased with the appearance of the crack. During the loading from the 2nd cycle of the 4% story drift (Δ = −53.6 mm) to the first cycle of the 5% story drift (Δ = +67 mm), the upper flange crack penetrated with a significant load drop when the load-displacement was −21 mm, and the test was declared over, as shown in Figure 7a.
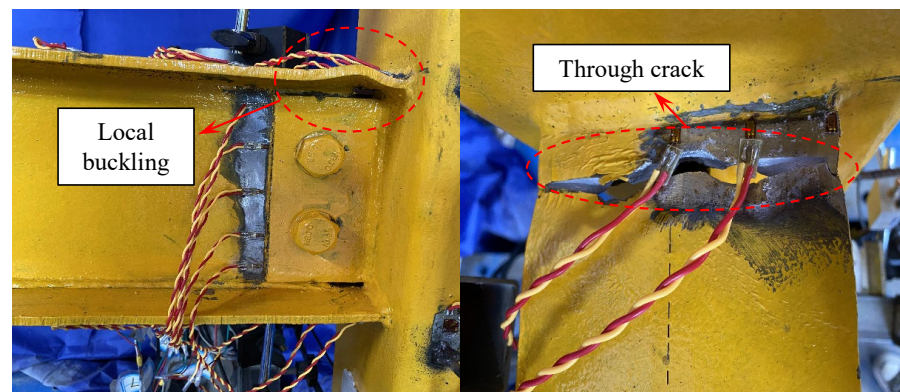
3.2. RBS Specimen

Before loading to the 4% story drift, the test phenomenon of the RBS specimen was similar to that of the BASE specimen. When loaded to the 4% story drift (Δ = +53.6 mm), the paint wrinkles were more evident than in the previous stages. By increasing the loading cycle in the first cycle of the 5% story drift (Δ = +67 mm), local buckling occurred in the weakened upper flange because of compression, meanwhile, the slippage occurred in the web bolt-connection area. In the first cycle of the 6% story drift (Δ = −80.4 mm), buckling deformation of the upper flange of the beam and a slight torsion of the beam occurred. During loading to the first cycle of the 7% story drift (Δ = +93.8 mm), the weld heat-affected zone of the upper flange cracked when load displacement was +56 mm, and the test was stopped with a sharply decreasing load. The failure mode of the RBS specimen is shown in Figure 7b.
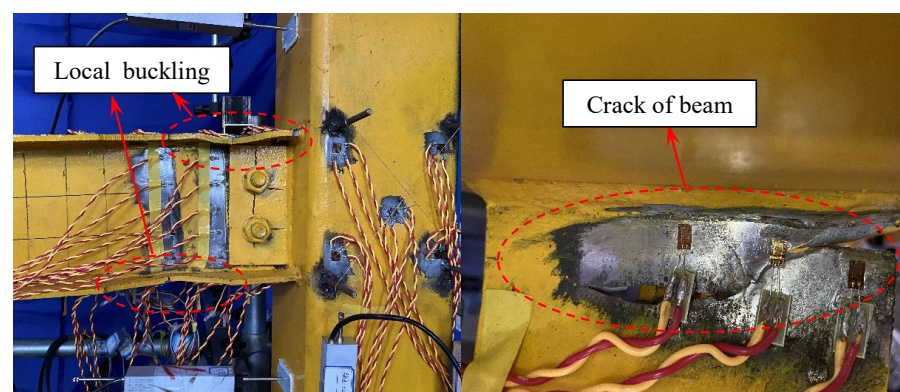
3.3. PRBS Specimen

The PRBS specimens were in an elastic state during the first three stages of the test. By increasing the loading cycle, in the second cycle of the 1% story drift (Δ = +13.4 mm), the load-displacement curve changed from the original linear trend to a fusiform envelope surface, which marked the beginning of the plastic stage of the specimen. At a 1.5–2% story drift, the envelope shape of the test load-displacement curve and the test phenomenon of the specimen indicated that the plasticity of the PRBS specimen was fully developed with no slippage at this stage of the bolt connection. At the first cycle of 3% story drift (Δ = +40.2 mm), the bolt slipping sounds occurred, the slippage of the bolt connection was observed in the flange-splicing area, and local buckling occurred on the flange of the dog-bone-style splice section near the side of the short beam. Simultaneously, the load-displacement curve began to show a serrated mutation and tended to be stable during subsequent loading, as shown in Figure 8. As the reciprocating displacement load was applied, slippage in the splicing section and local buckling occurred. At the first cycle of the 7% story drift (Δ = +93.8 mm), the net section of the flange bolt hole of the dog-bone-style splice section broke when load displacement was −93.8 mm, and the test was completed. The failure modes of the PRBS specimens are shown in Figure 7c.

3.4. PRBS-R Specimen

The phenomenon of the PRBS-R specimen in the test process showed no evident change from that of the PRBS specimen; the difference was that the slippage of the PRBS-R specimen in the high-strength bolt connection was more uniform than that of the PRBS specimen, resulting in a smoother load–displacement curve for PRBS-R specimen, as shown in Figure 8. The final failure mode of the PRBS-R specimen was the fracture of the net section of the upper flange bolt hole of the dog-bone-style splice section. The failure modes are shown in Figure 7d.
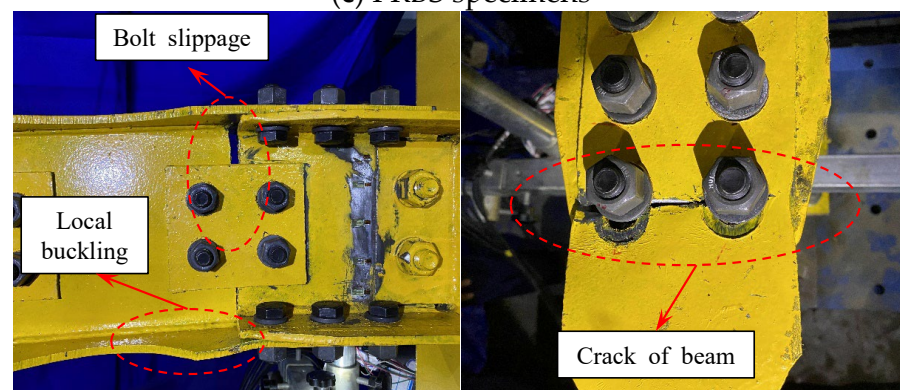
(**a**) BASE specimen

(**b**) RBS specimens

(**c**) PRBS specimens

(**d**) PRBS-R specimen

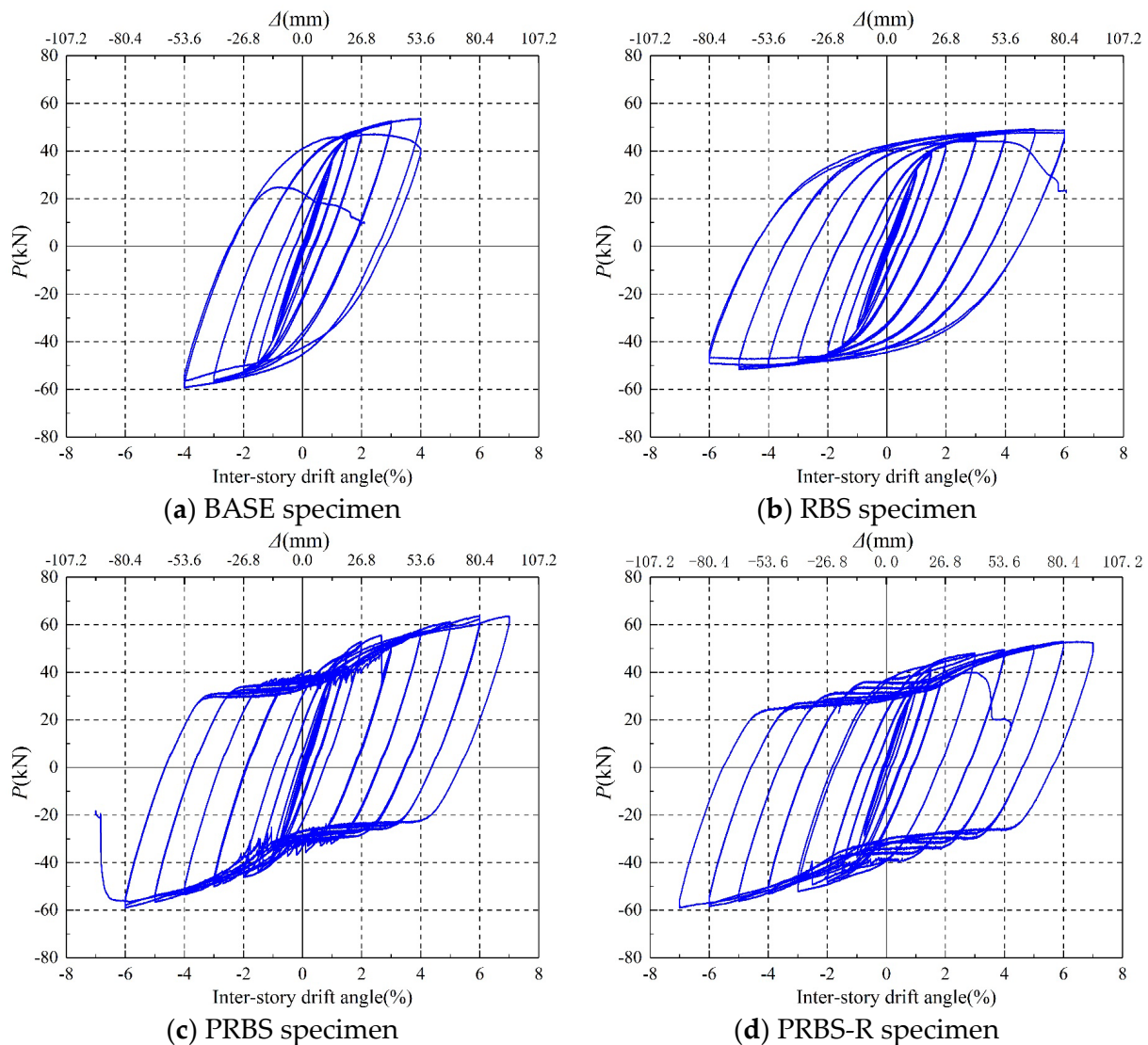**Figure 7.** Failure mode of specimens.

Figure 8. Hysteresis loops of specimens.

3.5. Failure Modes of Specimens

　　As for the BASE specimen, the flange of the beam near the surface of the column first yielded. With a gradual increase in loading displacement, the specimen completely lost its bearing capacity with crack penetration. The specimen exhibited clear characteristics of brittle failure. Unlike the BASE specimen, the RBS specimen initially yielded in the bone-weakening region, with plastic deformation primarily concentrated there. With the increase in loading displacement, the plastic region gradually extended toward the column until a crack appeared in the weld and its heat-affected zone, leading to specimen failure. It is worth noting that the plasticity of the bone-weakening region had already extensively developed before specimen failure. The primary reason for cracks appearing in the weld and its heat-affected zone, rather than the vulnerable area, might be attributed to construction quality issues in the weld.

　　As for the failure modes of PRBS and PRBS-R specimens, during the initial phase of load testing, the weakest area was concentrated within the bone-weakening region which entered the yielding stage first. As the applied load increased, the bolt friction connection near the short beam experienced failure, with a slippage of the bolt connection, which rendered it the weakest area. As the loading progresses, the flange bolt-hole net section develops cracks due to the material's tensile limit being exceeded, culminating in failure. Thus the final failure modes of the PRBS and PRBS-R specimens were the fracture

of the flange bolt-hole net section of the dog-bone-style splice section and the plastic hinge occurring centrally in the dog-bone-style splice section. In addition, the test revealed that the energy dissipations of both the PRBS and PRBS specimens were mainly composed of the energy dissipations of the bolt slippage and plastic deformation of the dog-bone-style splice section.

4. Comparative Analysis of Results

4.1. Hysteresis Loop

The load-displacement hysteresis curves of the four specimens illustrated in Figure 8 indicate that the energy dissipation capacity of the remaining specimens was significantly better than that of the BASE specimens. In addition, for the PRBS and PRBS-R specimens, the plastic deformation of the dog-bone-style splice section and slippage of the bolt connection jointly dissipated energy, resulting in a higher rotational capacity and ductility of the novel connection joint.

A comparison of the hysteretic curves of the BASE and RBS specimens reveals their load-displacement curves were similar before the failure of the BASE specimen. However, because of the dog-bone-weakening structure of the flange, the bearing capacity of the RBS specimen was less than that of the BASE specimen, whereas the rotational capacity of the RBS specimen was better than that of the BASE specimen. The formation of a plastic hinge in the weakened dog-bone area could be observed in combination with the failure mode, which indicated that the purpose of plastic-hinge relocation of the RBS specimen was achieved. The plastic hinges formed in the weakened dog-bone area could prevent premature brittle fracture in the weld zone near the column under an earthquake load.

A comparison of the load-displacement curves of the RBS and PRBS specimens reveals that the hysteresis curve of the RBS specimen was fully spindle-shaped, and the energy dissipation was mainly through the plastic deformation of the plate. The load-displacement curve of the PRBS specimen showed a slender spindle shape in the early stage of loading and a full "Z" shape in the later stage of loading, indicating that the energy dissipation capacity in the later stage was better than that in the early stage. The main reason was that in the early stage of the test, the specimen energy dissipation was mainly achieved through the plastic deformation of the plate, but after the slippage of the bolt connection, the plastic deformation of the plate and the slippage of the bolt connection jointly dissipated energy. The load–displacement curve shows that the ductility of the PRBS specimen was better than that of the RBS specimen owing to the existence of the bolt connection slippage.

The shapes of the load-displacement curves of the PRBS and PRBS-R specimens were similar; however, the bearing capacity of the PRBS-R specimen was slightly lower than that of the PRBS specimen, mainly because the contact surface of the splicing area was worn with the application of a reciprocating load in the first test. The test results indicated that the repaired PRBS connection joint exhibited good seismic performance. Furthermore, the failure of the PRBS and PRBSR specimens was a net section fracture of the bolt connection. Both the plastic deformation of the plate and slippage of the bolt connection were fully developed before failure, implying that the damage mode of the PRBS and PRBSR specimens was ductile failure.

4.2. Skeleton Curve

The skeleton curves of the four specimens are shown in Figure 9. Before the failure of the BASE specimen, its skeleton curve was consistent with that of the PRBS. In addition, the RBS specimen showed good rotation ability compared with the BASE specimen, and owing to the dog-bone weakening of the flange, the bearing capacity of the RBS specimen was slightly lower than that of the BASE specimen.

Compared with the PRBS specimen, the skeleton curves of the PRBS and PRBS-R specimens exhibited the same trend, and both exhibited slip characteristics. However, owing to plastic damage in the first test, the bearing capacity of the PRBS-R specimen was lower than that of the PRBS specimen. Unlike the BASE and RBS specimens, after the bolt

slip was complete, the bolt and hole wall began to contact and squeeze each other, causing the bearing capacities of the PRBS and PRBS-R specimens to continue increasing.
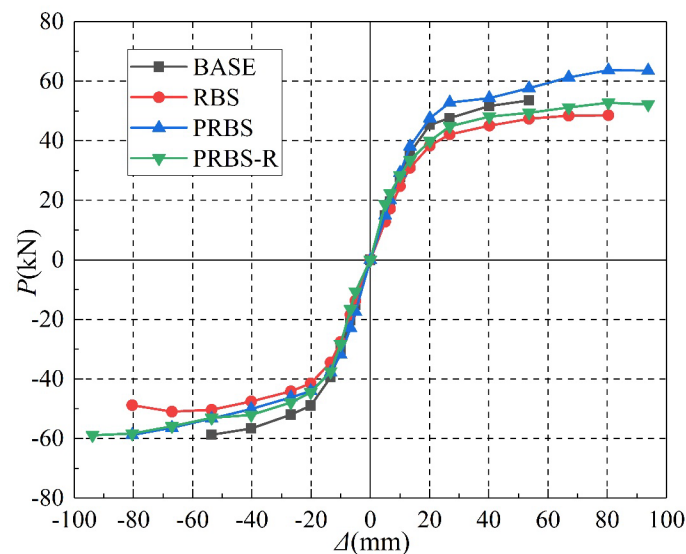

Figure 9. Skeleton curves of specimens.

4.3. Stiffness Degradation

During the test process, cyclic loading led to the accumulation of structural damage, and the structural stiffness decreased with an increase in the loading level. The secant stiffness of the first cycle of each loading stage was used to represent the structural stiffness at that stage [37]. The structural stiffness degradation curves of the specimens are presented in Figure 10.
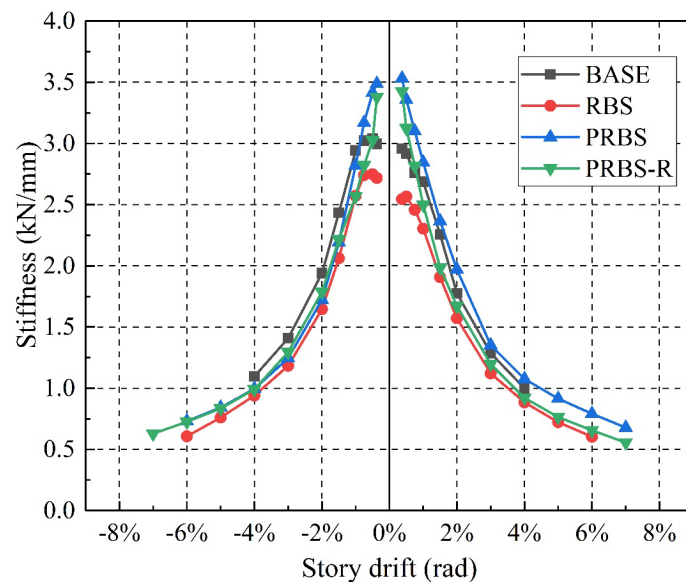

Figure 10. Stiffness degradation curves of specimens.

As shown in Figure 10, the stiffness of all the specimens consistently maintained a decreasing trend throughout the test. With an increase in the load stage, the specimens entered the hardening stage, and the stiffness degradation began to slow until the failure of the specimens. The main causes of stiffness degradation were the slippage of the bolt connection, buckling and plastic development of the beam, and accumulated damage to the specimens.

For the PRBS and PRBS-R specimens, the cantilever short beam was widened while designing the specimens to ensure that damage occurred in the dog-bone-style splice section. Therefore, the initial stiffness values of the PRBS and PRBS-R specimens were significantly higher than those of the BASE and RBS specimens. In addition, owing to the dog-bone weakening of the flange, the initial stiffness of the RBS specimen was lower than that of the BASE specimen.

4.4. Strain Distribution

During the test process, the strain of the panel zone did not exceed the steel yield strain; therefore, only the beam strain distribution is analyzed in this section.

Figures 11–13 show the strain distribution curves of the BASE, RBS, and PRBS specimens. The flange and web of the BASE specimens were in the elastic phase during the early stages of the test. With an increase in the load, the beam section near the column surface yielded first, implying that a plastic hinge was formed. The plastic deformation of the BASE specimen gradually accumulated until the beam section near the column surface cracked. For the RBS specimen, the first yielding of the flange occurred in the weakened region, indicating that the weakened beam flange could achieve plastic hinge relocation. However, the flange and web near the column surface yielded before the failure of the RBS specimen, indicating that damage did not occur only in the weakened region.
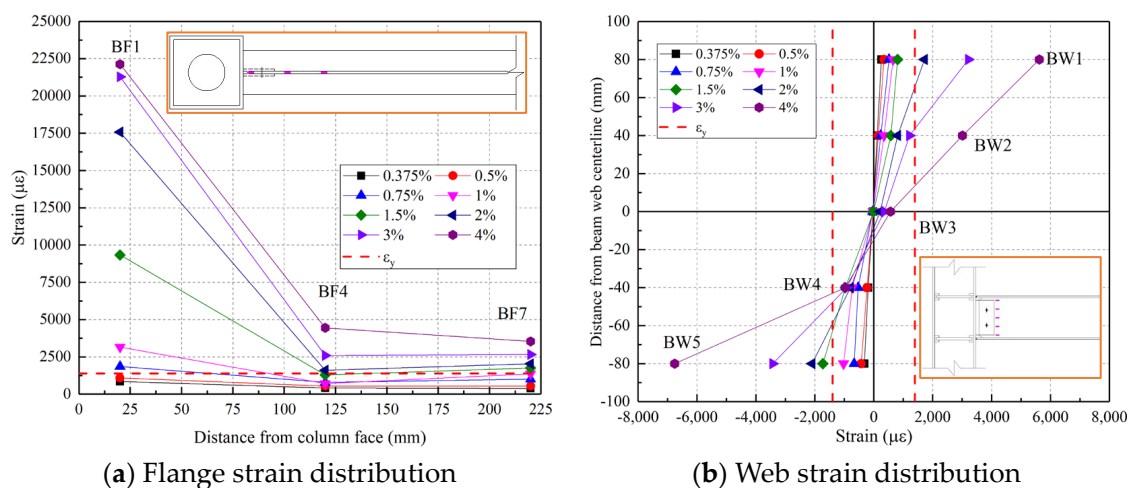

(**a**) Flange strain distribution   (**b**) Web strain distribution

Figure 11. Strain distribution of BASE specimen.

(**a**) Flange strain distribution   (**b**) Web strain distribution

Figure 12. Strain distribution of RBS specimen.
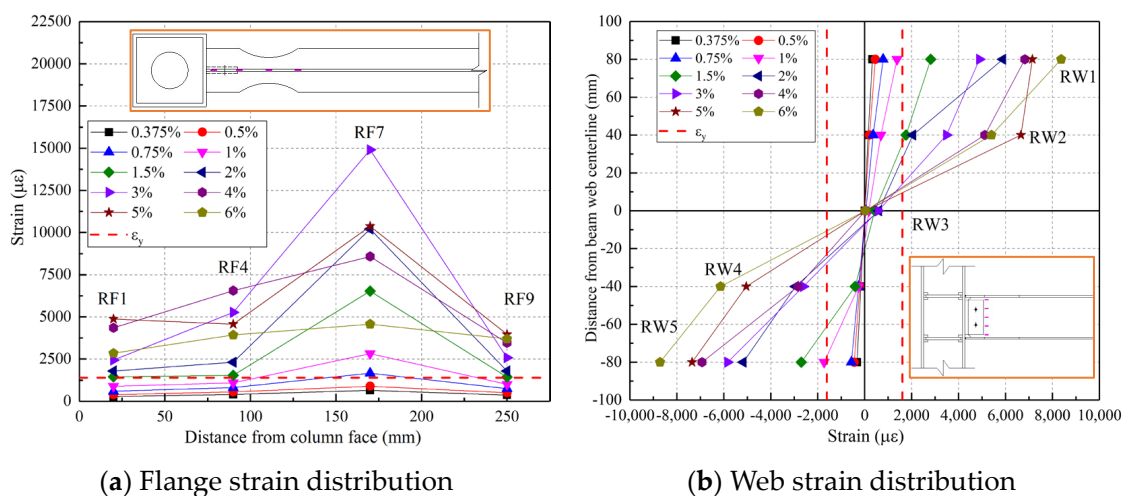
(**a**) Flange strain distribution   (**b**) Web strain distribution
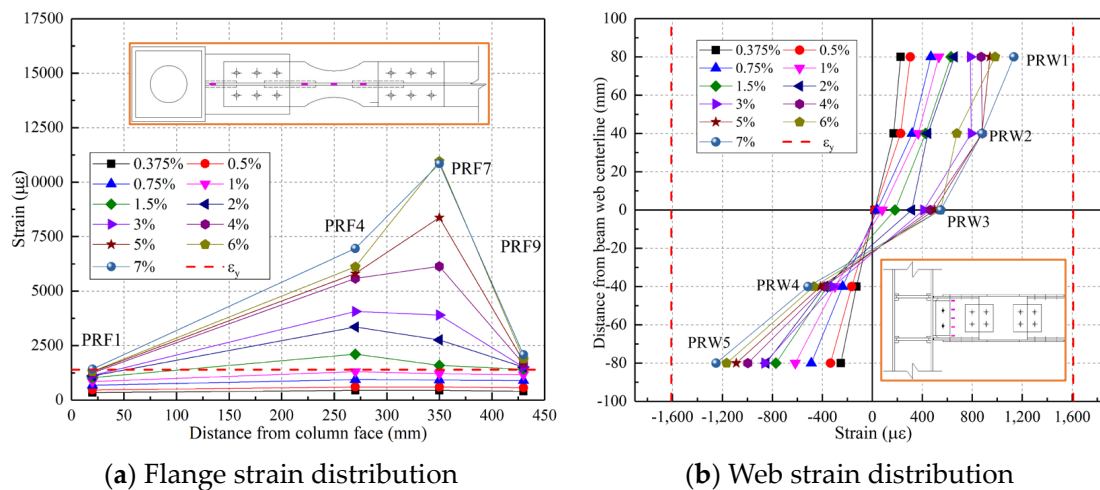
Figure 13. Strain distribution of PRBS specimen.

In addition, for the PRBS specimen, the cantilever beam did not reach the yield strain and remained elastic during loading. In the middle and late stages of the test, the strain in the dog-bone-style splice section reached the yield strain, indicating the formation of a plastic hinge. In addition, after the test, the damage was primarily concentrated in the dog-bone-style splice section, and the cantilever beam and H-beam did not exhibit plastic damage during loading, which provided conditions for rapid repair after the connection was destroyed.

4.5. Seismic Performance Index

The skeleton curves of all the specimens in the test were processed and analyzed, and the seismic performance indices of each specimen were obtained, including the yield displacement (Δ_y), yield load (P_y), peak load (P_m), ultimate displacement (Δ_u), and displacement ductility (μ). To eliminate the influence of asymmetric loading on the calculation results, the average values of the performance index parameters were considered for the analysis. The calculation results are listed in Table 2. The yield loads and displacements of the specimens were calculated using the general yield-bending moment method [38].

Table 2. Seismic performance index of specimens.

Specimen	Δ_y/mm	P_y/kN	P_m/kN	Δ_u/mm	μ
BASE	23.32	48.44	56.12	53.60	2.30
RBS	24.39	42.00	49.76	80.40	3.30
PRBS	26.11	49.14	61.23	87.10	3.33
PRBS-R	27.91	45.66	55.82	93.80	3.53

As shown in Table 2, the peak load of the PRBS specimen was the largest, indicating that the PRBS connection had a higher bearing capacity. In addition, even though the peak load of the PRBS-R specimen decreased by approximately 7.1% after repair, it was still greater than that of the RBS specimen, indicating that the repaired PRBS-R specimen retained a significant bearing capacity. Except for the BASE specimen, the displacement ductility exceeded 3.0, indicating that the novel connection had good ductility [39].

4.6. Energy Dissipation Capacity

Figure 14 shows the total energy dissipations of the specimens. The diagram shows that the BASE specimen had the lowest energy dissipation, mainly because premature damage to the BASE specimen occurred to the extent that its beam plasticity was not fully developed. In addition, the total energy dissipation of the RBS specimen was higher than

that of the BASE specimen, which was due to the local buckling in the bone-weakening area of the RBS specimen before failure, and the well-developed plasticity. Because of the local buckling and bolt slippage of the splicing section, the plasticity of the novel connection was fully developed, and the total energy dissipation was the highest. Compared with the BASE specimen, the total energy dissipations of RBS and PRBS specimens increased by 146.74% and 194.23%, respectively. Moreover, compared to the PRBS specimen, the energy dissipation of the RPRBS specimen was only reduced by 0.84%, which was caused by the initial imperfection of the repaired specimen.
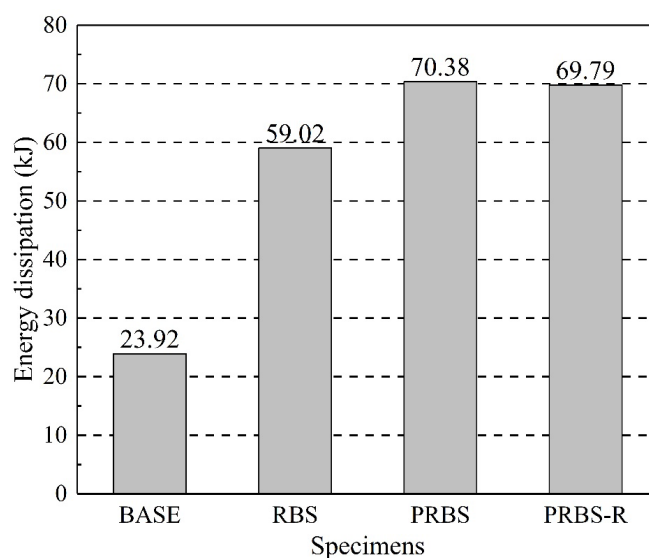

Figure 14. Energy dissipation of specimens.

5. Finite Element Analysis

5.1. Finite Element Model

In this study, the FE software ABAQUS 6.14 was used to model the BASE, RBS, and PRBS specimens. The model sizes were the same as those of the actual specimens. In the FE models, an eight-node solid element (C3D8R) was used to model the concrete, steel plate, and bolt [33,40]. To ensure that the force states of the models were consistent with those of the specimens, the model boundary conditions were consistent with those of the test, that is the hinge connection in the column top and bottom, lateral displacement limitation in the beam, displacement load applied to the beam end, axial load (300 kN) applied to the column top, and bolt load (100 kN for M16 bolts, 155 kN for M20 bolts) applied to the bolts. According to the literature [33], the mesh size of the beam was 15 mm after many trials and calculations, whereas that of the dog-bone-weakened area of the RBS and dog-bone-style splice section of the PRBS was 10 mm. The precast column was meshed to a size of 30 mm to improve computational efficiency. In addition, the multiple linear kinematic hardening mode was used to simulate the mechanical properties of steel. The strain-stress relationship of steel is shown in Figure 15a, where the values of f_y, f_u, E_s and ε_u were taken from Table 1. Furthermore, the concrete damage plasticity (CDP) mode was used to simulate the mechanical properties of concrete, as shown in Figure 15b. In the figure, f_{ck} is the standard value of axial compressive strength; f_{tk} is the standard value of axial tensile strength; ε_{ck} is the peak compressive strain of concrete and ε_{tk} is the peak tensile strain of concrete. The values of parameters and repeated unloading and reloading stress path of concrete were calculated by the method recommended in the literature [33].

The contact between concrete and square still tube, steel plate and steel plate, and bolt and steel plate were simulated using "surface-to-surface contact" provided by ABAQUS, which includes normal and tangential contact. The normal and tangential contact were simulated using "hard contact" and the Coulomb friction model, respectively. The friction coefficient between steel and concrete was taken as 0.25 [33], and the friction coefficient

between steels was taken as 0.31, which was obtained from an anti-slip test. Nonlinear geometric deformations were considered in the FE model. The mesh and boundary conditions of the model are shown in Figure 16.
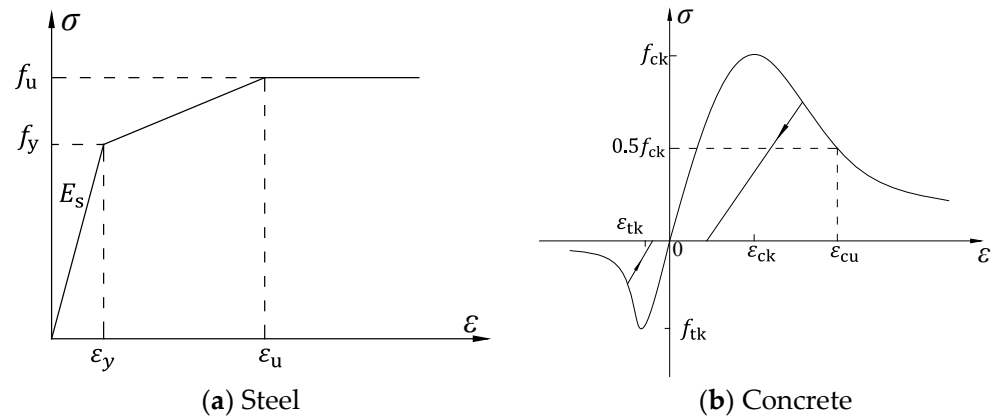

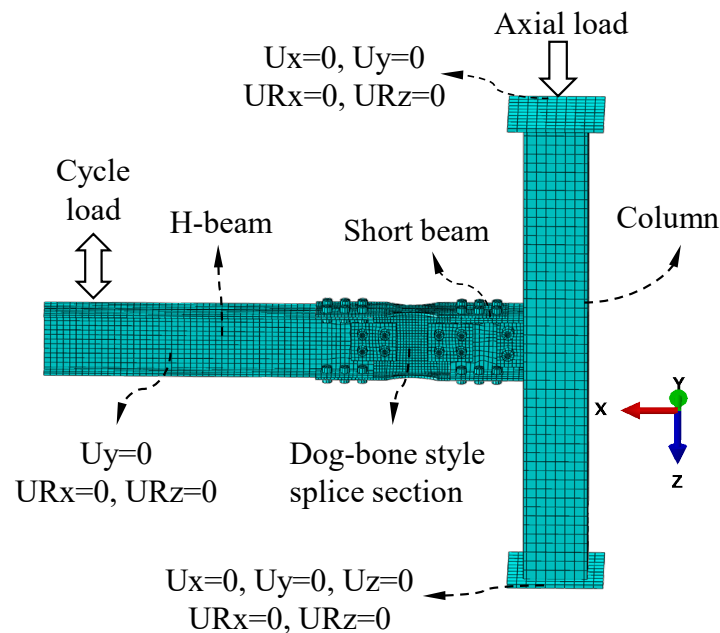**Figure 15.** The strain-stress relationship of steel and concrete.

Figure 16. FE model of PRBS specimen.

5.2. Model Verification

A comparison of the deformation and plastic strain distribution between the FE model and the experimental test is shown in Figure 17. The figures unequivocally demonstrate that the FE models formulated in this study accurately reproduced the mechanical behavior and failure mode of the specimens. In the BASE model, plastic deformation and local buckling were initially manifested in the beam flange adjacent to the column. Under progressive loading, the plastic deformation escalated and extended outward, culminating in the formation of a plastic hinge at this location. Consequently, the beam flange near the column fractured, resulting in brittle failure.

In the RBS model, plastic deformation and local buckling initially occurred in the weakened flange. With the continued loading, the plastic region gradually extended towards the beam flange adjacent to the column, with the plastic hinge mainly concentrated in the weakened area. Ultimately, failure occurred in the weakened region of the flange, effectively achieving the objective of plastic hinge relocation and postponing structural failure.
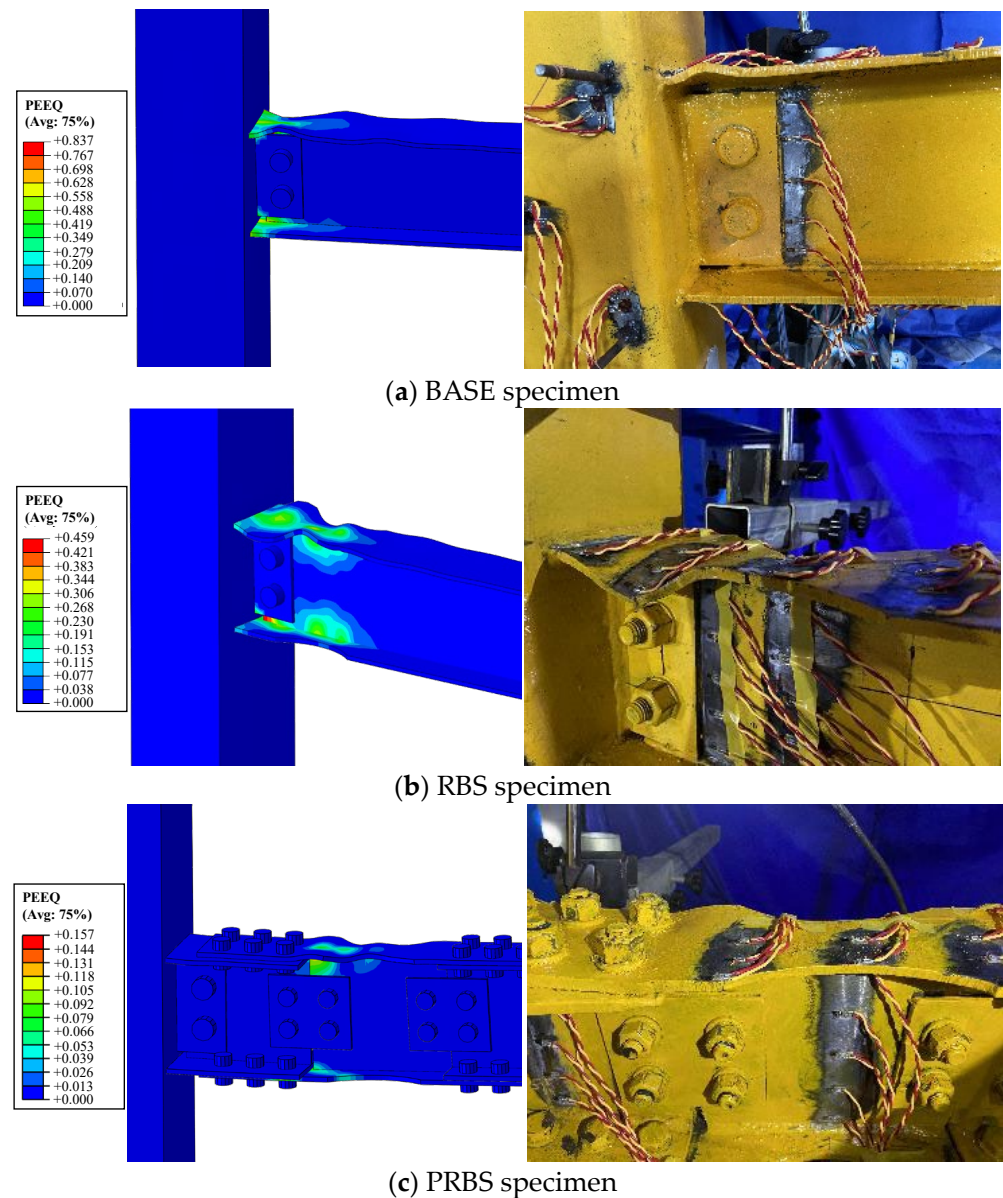
(**a**) BASE specimen

(**b**) RBS specimen

(**c**) PRBS specimen

Figure 17. Comparison of the failure modes of the test and FE.

In sharp contrast to the BASE and RBS models, the PRBS model initially exhibited plastic deformation and local buckling in the splice section. As the loading progressed, plastic deformation was predominantly concentrated in the splice section, which was consistent with the strain measurement data. Furthermore, the graph shows that the PRBS model, apart from the dog-bone-style splice section, remains in the elastic stage. Consequently, the swift restoration of the PRBS structure can be accomplished by replacing the dog-bone-style splice section. The PRBS connection effectively achieves the objectives of plastic hinge relocation, postponing structural failure, and post-earthquake rapid repair.

Hysteresis loops comparing the finite FE model with the test results are shown in Figure 18. The figures exhibit a notable agreement between the hysteresis loops of the FE models and test results, confirming the accurate prediction of the stiffness and bearing capacity of the specimens using the FE model. These comparison results indicate the suitability of the FE model established in this study for further investigation of this specific type of joint.
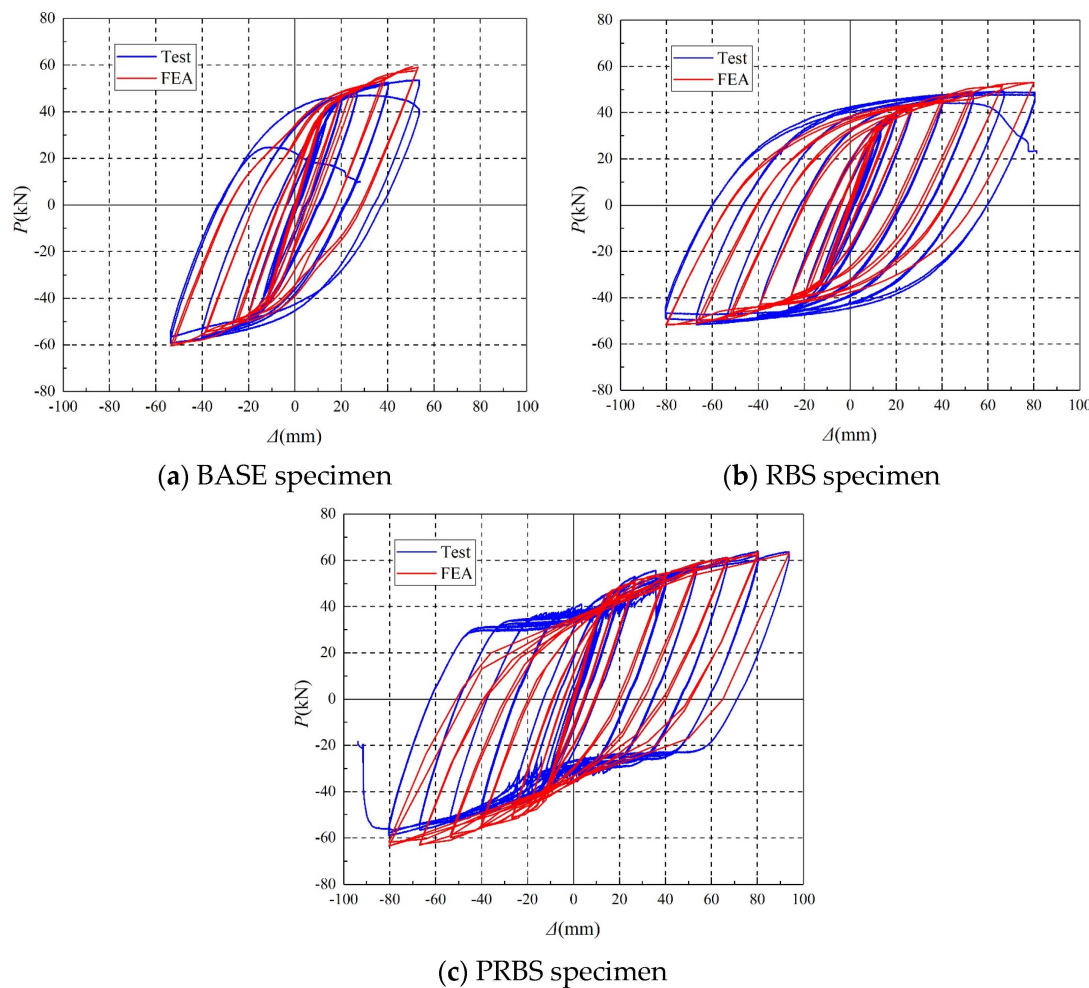
(**a**) BASE specimen

(**b**) RBS specimen

(**c**) PRBS specimen

Figure 18. Comparison of the hysteresis loops of the test and FE.

5.3. Parametric Analysis

To investigate the influence of the dog-bone-style flange-weakening width, splice-section flange thickness, and flange bolt diameter on the load-bearing capacity of the PRBS connection, 15 finite element models were developed for parametric analysis using the ABAQUS software. All models were created using the methodology described in Section 5.1. To expedite computational efficiency, monotonic loading was applied to all the models. The model parameters are listed in Table 3 and are named as "P-D-t_f-d_b", where D represents the weakening width, t_f denotes the flange thickness, d_b denotes the flange bolt diameter, d_h denotes the bolt hole diameter and its value for various bolt types is dictated by the relevant code [31], as depicted in Figure 19. The skeleton curves and performance indices of the models are shown in Figure 20 and Table 4, respectively.

Figure 20a and Table 4 show that with a gradual increase in the weakening width, both the ultimate and yield loads of the models decrease progressively. As the weakening width increased from 0 to 35 mm, the ultimate load and yield load experienced a reduction of 9.09% and 20.46%, respectively. The decrease in yield load was mainly attributed to an increase in the weakening depth, which modified the model's yield mode. This alteration shifted the location of yield from the bolt splice connection to the bone-weakening section, resulting in an earlier initiation of the yield phase and a subsequent reduction in the model's yield load. Furthermore, as the increase in the weakening depth did not alter the model's ultimate failure mode, its impact on the model's ultimate load was relatively minor.

Figure 20b and Table 4 show that with a gradual increase in the flange thickness, both the ultimate and yield loads of the models progressively increase. Compared with

the weakening width, the influence of the flange thickness on the load-bearing capacity of the model was more pronounced. As the flange thickness increased from 4 mm to 12 mm, the ultimate load experienced a significant increase of 114.33%. This substantial increase was mainly attributed to the enhancement of the overall flexural stiffness of the weakened section owing to the increased flange thickness. Consequently, the load-bearing capacity at the weakest interface improved. Under the effect of beam-end loading, the plastic deformation at the weakening section diminished with an increase in the flange thickness, leading to an increase in the load-bearing capacity of the model.

Figure 20c and Table 4 show that with an increase in the bolt diameter, both the ultimate and yield loads of the models first increased and then decreased. The maximum load-bearing capacity was achieved when the flange bolt diameter was 14 mm. The primary reason for this behavior was the change in the failure mode of the model with varying bolt diameters. When the flange bolt diameters were 12 and 14 mm, the failure mode of the model was compression failure of the flange bolt hole wall. Consequently, the load-bearing capacity increased with the bolt diameter. However, when the flange bolt diameter exceeded 14 mm, the failure mode of the model was tension damage to the splicing section flange at the bolt. This resulted in a decrease in load-bearing capacity with an increase in the bolt diameter.

Table 3. Characters of FE models.

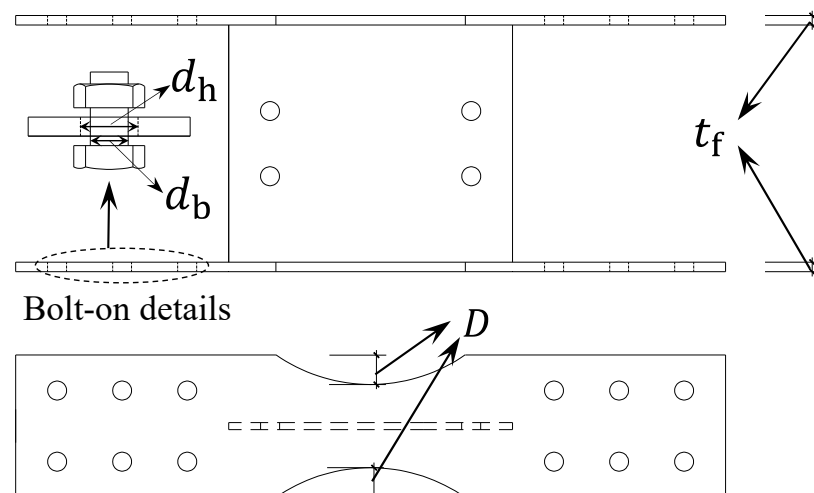| Model	Weakening Width D/mm	Flange Thickness t_f/mm	Flange Bolt Diameter d_b/mm	Bolt Hole Diameter d_h/mm
P25-8-16	25	8	16	17.5
P0-8-16	0	8	16	17.5
P5-8-16	5	8	16	17.5
P10-8-16	10	8	16	17.5
P15-8-16	15	8	16	17.5
P20-8-16	20	8	16	17.5
P30-8-16	30	8	16	17.5
P35-8-16	35	8	16	17.5
P25-4-16	25	4	16	17.5
P25-6-16	25	6	16	17.5
P25-10-16	25	10	16	17.5
P25-12-16	25	12	16	17.5
P25-8-12	25	8	12	13.5
P25-8-14	25	8	14	15.5
P25-8-18	25	8	18	20.0
P25-8-20	25	8	20	22.0

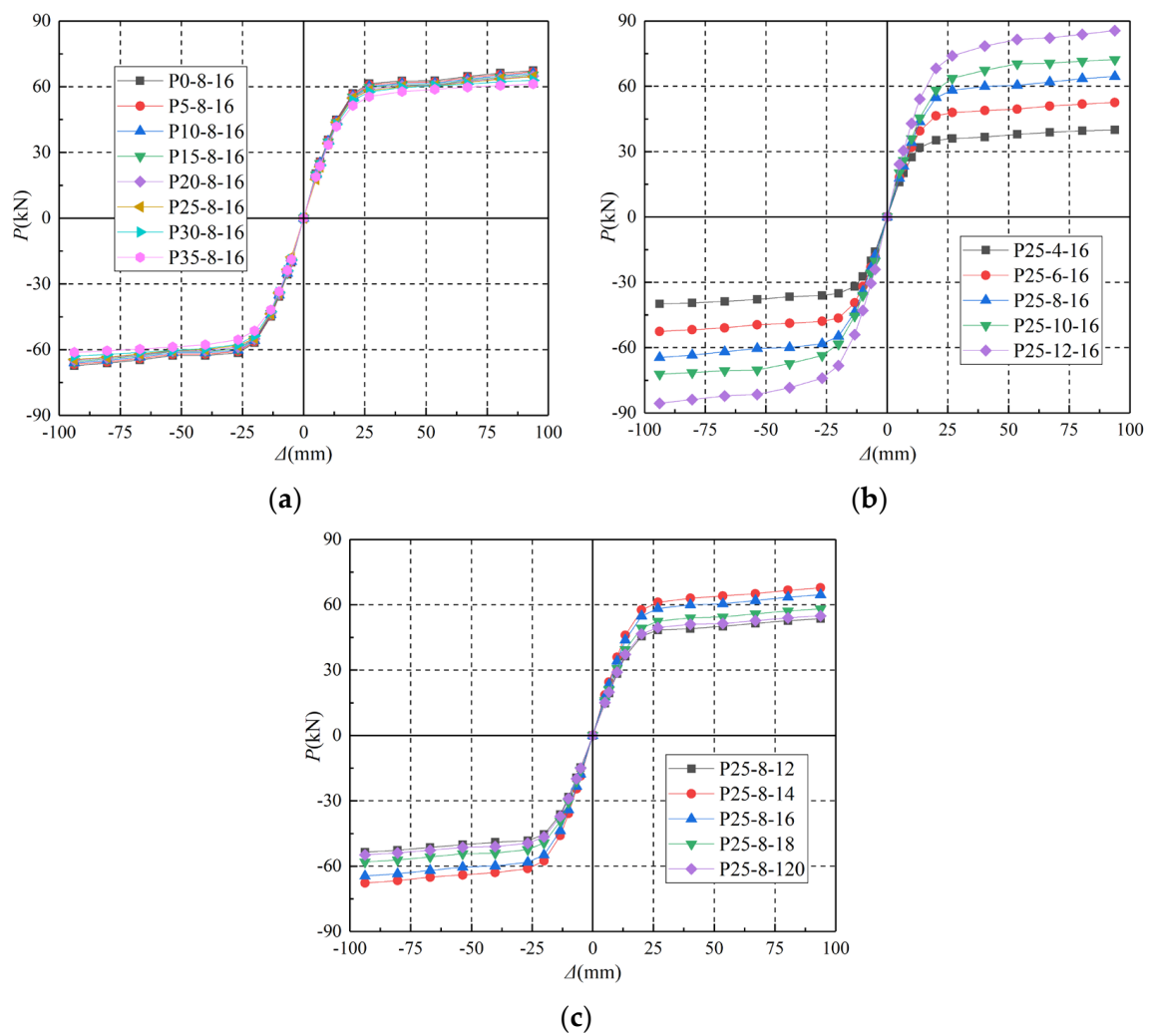**Figure 19.** Research parameters of the splice section.

Figure 20. Skeleton curves of FE models. (**a**) Skeleton curves of different weakening widths. (**b**) Skeleton curves of different flange thicknesses. (**c**) Skeleton curves of different bolt diameters.

Table 4. Comparison between FE and theoretical analyses.

FE Model	FE Value		Calculated Value		Error	
	P_{ye}/kN	P_{ue}/kN	P_{yc}/kN	P_{uc}/kN	δy	δu
P25-8-16	51.06	64.53	47.22	64.08	−7.53%	−0.70%
P0-8-16	52.35	67.35	52.92	64.08	1.08%	−4.85%
P5-8-16	52.01	66.69	52.92	64.08	1.74%	−3.92%
P10-8-16	51.96	66.04	52.92	64.08	1.84%	−2.97%
P15-8-16	51.45	65.39	52.92	64.08	2.86%	−2.00%
P20-8-16	50.12	64.76	51.95	64.08	3.65%	−1.06%
P30-8-16	46.76	62.98	42.48	64.08	−9.15%	1.75%
P35-8-16	41.64	61.22	37.75	64.08	−9.35%	4.67%
P25-4-16	30.53	39.92	27.88	36.90	−8.69%	−7.56%
P25-6-16	40.96	52.56	38.69	50.36	−5.53%	−4.19%
P25-10-16	55.77	72.25	55.90	78.06	0.23%	8.04%
P25-12-16	59.12	85.56	64.74	92.30	9.52%	7.87%
P25-8-12	45.36	53.56	43.58	58.27	−3.93%	8.79%
P25-8-14	51.65	67.76	47.22	66.90	−8.58%	−1.27%
P25-8-18	45.35	58.08	47.22	61.06	4.12%	5.15%
P25-8-120	42.62	54.85	47.22	57.29	10.79%	4.46%

6. Bearing Capacity for the PRBS Connection

This section considers the PRBS specimen as the research object and analyzes the possible yielding and damage modes of the PRBS connection based on the test measurement data and the observed damage phenomena; thus, a simplified calculation method for the yielding bearing and ultimate bearing capacities of the PRBS connection is presented. In addition, the calculated results were compared with the experimental results. A schematic of the calculation is presented in Figure 21.
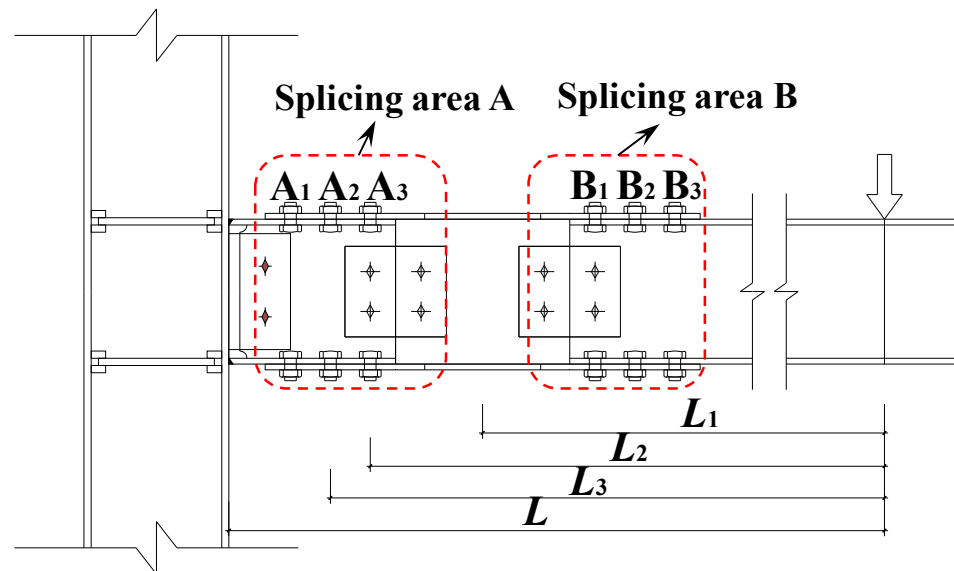

Figure 21. Calculation sketch for the bearing capacity. In the figure, A and B denote the splicing area, A_1–A_3, B_1–B_3 denote the flange bolt numbers, L and L_1–L_3 denote the distance between the loading point and the locations in the figure.Calculation of the yield-bearing capacity.

When the specimens were designed before the test, to avoid the risk of beam-column welding failure, the cantilevered short beam flange was widened to ensure that the probable maximum moment at the face of the column section (M_f) was less than the plastic moment of the beam based on the expected yield stress (M_{pe}) [32,33], such that the yielding and damage of the beam section at the face of the column occurred later than that of the weakened dog-bone section. According to the force mechanism, the plasticity of the PRBS connection joint may be caused by several scenarios: (1) yielding of the dog-bone-weakened section (P_{y1}), (2) yielding of the splice section flange at the A3 row of bolts (P_{y2}), (3) yielding of the flange bolt-hole wall by compression at splice area A (P_{y3}), and (4) yielding of the flange bolt screw by shear at splice area A (P_{y4}). The load at the time of possible yielding is calculated separately, and the minimum value is taken as the yield-bearing capacity (P_y). The formula is as follows:

$$P_{y1} = W_e f_y / L_1, \tag{5}$$

$$P_{y2} = [b_f t_f f_y (h - t_f) + n_1 \alpha_1 P \mu (h - 2t_f)/2]/L_2, \tag{6}$$

$$P_{y3} = [d t_f f_y (h - t_f) + \alpha_1 P \mu (h - 2t_f)] n / L_3, \tag{7}$$

$$P_{y4} = \left[A_{eff} f_v^b (h - t_f) + \alpha_1 P \mu (h - 2t_f) \right] n / L_3 \tag{8}$$

$$P_y = min\{P_{y1}, P_{y2}, P_{y3}, P_{y4}\} \tag{9}$$

where W_e is the elastic section modulus of the dog-bone-reduced section; f_y is the yield strength of the steel plate; b_f is the flange width of the splicing section in Area A; t_f is the flange thickness of the splicing section in Area A; h is the height of the dog-bone-style splice section; n_1 is the number of single-side flange bolts at the calculated section; α_1 is the reduction coefficient of the bolt friction, which is 0.7 [41]; P is the bolt preload; μ is the friction coefficient; d is the diameter of the screw hole; n is the number of bolts distributed on the upper or lower flange in Area A; A_{eff} is the effective cross-sectional area at the thread; f_y^b is the yield strength of bolt and f_v^b is the shear strength of the bolt, where $f_v^b = 0.58 f_y^b$ [42].

1. Calculation of the Ultimate Bearing Capacity

With an increase in the load, the failure of the PRBS connection joint may be caused by several scenarios: (1) plastic failure of the dog-bone-weakened section (P_{u1}), (2) tension damage of the splicing section flange at the A3 row bolt (P_{u2}), (3) compression failure of the flange-bolt hole wall in splicing area A (P_{u3}), and (4) shear failure of the flange bolt screw at splicing area A (P_{u4}). The load at the time of possible failure was calculated separately, and the minimum value was considered the ultimate bearing capacity (P_u). The formula is as follows:

$$P_{u1} = \frac{W_u f_u}{L_1} \tag{10}$$

$$e_f = I / I_f \tag{11}$$

$$P_{u2} = [(b_f - 2d) t_f f_u (h - t_f)] e_f / L_2 \tag{12}$$

$$P_{u3} = [d t_f f_u (h - t_f)] n e_f / L_3 \tag{13}$$

$$P_{u4} = \left[0.58 A_{eff} f_u^b (h - t_f) \right] n e_f / L_3 \tag{14}$$

$$P_u = min\{P_{u1}, P_{u2}, P_{u3}, P_{u4}\} \tag{15}$$

where W_u is the plastic section modulus of the dog-bone-reduced section, f_u is the ultimate strength of the steel plate, I is the moment of inertia of the calculated section, I_f is the moment of inertia of the calculated section flange, and f_u^b is the ultimate strength of the bolt.

The theoretical analysis results were compared with the experimental and FE analysis results, as shown in Tables 4 and 5 and Figure 22. Table 5 and Figure 22 show that the experimental and theoretical results for the PRBS specimen exhibit a satisfactory agreement, with an error of less than 5%. However, for the PRBS-R specimen, the yield-bearing capacity error is 3.40%, whereas the ultimate bearing capacity error is 14.8%. The primary reason for this discrepancy is that the PRBS-R specimen was a repair specimen with initial imperfections prior to testing, resulting in a noticeably lower ultimate load than the PRBS specimen. An analysis of Table 4 and Figure 22 reveals that the errors in yield-bearing and ultimate bearing capacities between the FE and theoretical analyses were predominantly below 10%. Consequently, these results suggest that the theoretical analysis aligns well with both the experimental and FE analyses.

Table 5. Comparison between experimental and theoretical analyses.

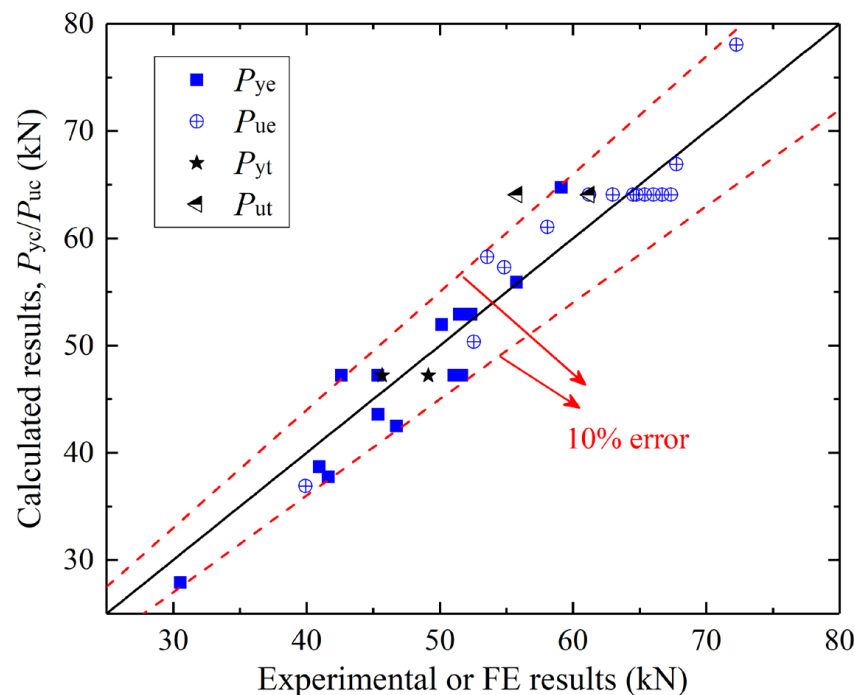| Specimen	Experimental Value		Calculated Value		Error	
	P_{yt}/kN	P_{ut}/kN	P_{yc}/kN	P_{uc}/kN	δy	δu
PRBS	49.14	61.23	47.22	64.08	−3.91%	4.65%
PRBS-R	45.66	55.82	47.22	64.08	3.40%	14.80%

Figure 22. Comparison of theoretical analysis with experimental and FE analyses.

7. Conclusions

In this study, a precast reduced beam section connection joint with a dog-bone-style splice section was proposed, and quasi-static tests and FE analyses were conducted on welded flange-bolted web connection joints, traditional bone-weakened joints, PRBS connection joints, and repaired PRBS connection joints. The following conclusions are drawn from the comparative analysis:

(1) Compared with the BASE and RBS connection joints, the PRBS connection had a higher bearing capacity, ductility, and energy dissipation capacity. The energy dissipation of the PRBS connection was realized by bolt slippage and plastic deformation of the dog-bone-style splice section. Moreover, the novel connection could effectively relocate the plastic hinge and cause plastic damage concentrated in the dog-bone-style splice section.

(2) After the test, the main components of the PRBS connection were undamaged, resulting in a rapid repair of the joint. In addition, the repaired PRBS still exhibited stable mechanical properties, which could ensure the safe service of the overall structure.

(3) The FE model formulated in this study demonstrated excellent accuracy in predicting the mechanical behavior, failure mode, stiffness, and bearing capacity of the specimens. Furthermore, the results of the parametric analysis revealed that the flange thickness exerted the most significant influence on the load-bearing capacity of the model. The load-bearing capacity of the model was negatively correlated with the weakening width but positively correlated with the flange thickness. Moreover, as the flange bolt diameter increased, the load-bearing capacity of the model initially increased and then decreased.

(4) Based on the experimental data and observed failure phenomena, the possible yield and damage modes of the PRBS connection were analyzed, and a simplified calculation method for the yield and ultimate bearing capacities of the PRBS connection was proposed. The calculation results were in good agreement with the experimental results.

References

1. Tremblay, R.; Timler, P.; Bruneau, M.; Filiatrault, A. Performance of steel structures during the 1994 Northridge earthquake. *Can. J. Civ. Eng.* **1995**, *22*, 338–360. [CrossRef]
2. Xu, Q.; Chen, H.R.; Li, W.Y.; Zheng, S.S.; Zhang, X.H. Experimental investigation on seismic behavior of steel welded connections considering the influence of structural forms. *Eng. Fail. Anal.* **2022**, *139*, 106499. [CrossRef]
3. Fanaie, N.; Nadalipour, Z.; Sarkhosh, O.S.; Faegh, S.S. Elastic drift amplification factor in steel moment frames with double reduced beam section (DRBS) connections. *J. Build. Eng.* **2021**, *43*, 102563. [CrossRef]
4. Horton, T.A.; Hajirasouliha, I.; Davison, B.; Ozdemir, Z. More efficient design of reduced beam sections (RBS) for maximum seismic performance. *J. Constr. Steel Res.* **2021**, *183*, 106728. [CrossRef]
5. Mansouri, A.; Shakiba, M.R.; Fereshtehpour, E. Two novel corrugated web reduced beam section connections for steel moment frames. *J. Build. Eng.* **2021**, *43*, 103187. [CrossRef]
6. Deylami, A.; Tabar, A.M. Promotion of cyclic behavior of reduced beam section connection restraining beam web to local buckling. *Thin Walled Struct.* **2013**, *73*, 112–120. [CrossRef]
7. Chen, S.J.; Yeh, C.H.; Chu, J.M. Ductile steel beam-to-column connections for seismic resistance. *J. Struct. Eng.* **1996**, *122*, 1292–1299. [CrossRef]
8. Lee, C.H.; Jeon, S.W.; Kim, J.H.; Uang, C.M. Effects of panel zone strength and beam web connection method on seismic performance of reduced beam section steel moment connections. *J. Struct. Eng.* **2005**, *131*, 1854–1865. [CrossRef]
9. Paul, S.; Deb, S.K. Experimental study on a new V-cut RBS and CFT connections with bidirectional bolts under cyclic loadings. *J. Build. Eng.* **2022**, *46*, 103688. [CrossRef]
10. Tabar, A.M.; Alonso-Rodriguez, A.; Tsavdaridis, K.D. Building retrofit with reduced web (RWS) and beam (RBS) section limited-ductility connections. *J. Constr. Steel Res.* **2022**, *197*, 107459. [CrossRef]
11. Xu, Y.; Dai, Y.; Jia, Y.L. Study on the mechanical performances of aluminum assembled hub joints under axial loads. *J. Build. Eng.* **2022**, *50*, 104147. [CrossRef]
12. Zhang, R.J.; Zhang, Y.; Li, A.Q.; Yang, T.Y. Experimental study on a new type of precast beam-column joint. *J. Build. Eng.* **2022**, *51*, 104252. [CrossRef]
13. Li, S.; Xu, T.T.; Ding, S.H.; Li, X.L.; Guo, H.C.; Liu, Y.H. Seismic performance of a new assembled beam-column joint with cantilever beam splicing. *J. Constr. Steel Res.* **2022**, *196*, 107432. [CrossRef]
14. Oh, S.H.; Kim, Y.J.; Ryu, H.S. Seismic performance of steel structures with slit dampers. *Eng. Struct.* **2009**, *31*, 1997–2008. [CrossRef]
15. Soltanabadi, R.; Farhad, B. Experimental studies on a combined damper for repairable steel moment connections. *Int. J. Steel Struct.* **2018**, *18*, 211–224. [CrossRef]
16. Huang, L.; Sun, Q.; Deng, P.; Zhang, M.L.; Shan, R.; Peng, B. Study on seismic behavior of earthquake-damaged frame structures with rapid reversibility. *Build. Struct.* **2021**, *51*, 81–87. (In Chinese)
17. Ma, Z.H.; Zhang, J.G.; Liang, H.Z.; Li, L.Y. Numerical research on prefabricated frame joint based on artificial dissipative plastic hinge under low-reversed loading. *China Civ. Eng. J.* **2020**, *53* (Suppl. S2), 162–168. (In Chinese)
18. Ye, J.F.; Yan, G.Y.; Liu, R.Y.; Xue, P.R.; Wang, D. Hysteretic behavior of replaceable steel plate damper for prefabricated joint with earthquake resilience. *J. Build. Eng.* **2022**, *46*, 103714. [CrossRef]
19. Zhang, A.L.; Wang, Q.; Jiang, Z.Q.; Yang, X.F.; Zhang, H. Experimental study of earthquake-resilient prefabricated steel beam-column joints with different connection forms. *Eng. Struct.* **2019**, *187*, 299–313. [CrossRef]
20. Jiang, Z.Q.; Yang, X.F.; Dou, C.; Pi, Y.L.; Li, R. Design theory of earthquake-resilient prefabricated beam-column steel joint with double flange cover plates. *Eng. Struct.* **2020**, *209*, 110005. [CrossRef]
21. Zhang, H.; Su, M.Z.; Lian, M.; Cheng, Q.Q.; Guan, B.L.; Gong, H.X. Experimental and numerical study on the seismic behavior of high-strength steel framed-tube structures with end-plate-connected replaceable shear links. *Eng. Struct.* **2020**, *223*, 111172. [CrossRef]

22. Özkılıç, Y.O.; Bozkurt, M.B. Numerical validation on novel replaceable reduced beam section connections for moment-resisting frames. *Structures* **2023**, *50*, 63–79. [CrossRef]

23. Özkılıç, Y.O. A new replaceable fuse for moment resisting frames: Replaceable bolted reduced beam section connections. *Steel Compos. Struct.* **2020**, *35*, 353–370.

24. Özkılıç, Y.O.; Bozkurt, M.B.; Topkaya, C. Mid-spliced end-plated replaceable links for eccentrically braced frames. *Eng. Struct.* **2021**, *237*, 112225. [CrossRef]

25. Özkılıç, Y.O. Optimized stiffener detailing for shear links in eccentrically braced frames. *Steel Compos. Struct.* **2021**, *39*, 35–50.

26. Özkılıç, Y.O. Interaction of flange and web slenderness, overstrength factor and proposed stiffener arrangements for long links. *J. Constr. Steel Res.* **2022**, *190*, 107150. [CrossRef]

27. Özkılıç, Y.O.; Topkaya, C. Extended end-plate connections for replaceable shear links. *Eng. Struct.* **2021**, *240*, 112385. [CrossRef]

28. Özkılıç, Y.O. Cyclic and monotonic performance of stiffened extended end-plate connections with large-sized bolts and thin end-plates. *Bull Earthq. Eng.* **2022**, *20*, 7441–7475. [CrossRef]

29. Özkılıç, Y.O.; Un, E.M.; Topkaya, C. Frictional mid-spliced shear links for eccentrically braced frames. *Earthq. Eng. Struct. Dyn.* **2023**, 1–22. [CrossRef]

30. Özkılıç, Y.O. Cyclic and monotonic performance of unstiffened extended end-plate connections having thin end-plates and large-bolts. *Eng Struct.* **2023**, *281*, 115794. [CrossRef]

31. *GB/50017-2017*; Standard for Design of Steel Structures. National Standards of the People's Republic of China. China Architecture & Building Press: Beijing, China, 2017. (In Chinese)

32. *AISC/ANSI 358-16*; Prequalified Connections for Special and Intermediate Steel Moment Frames for Seismic Applications. American Institute of Steel Construction (AISC): Chicago, IL, USA, 2016.

33. Qi, H.; Hu, S.W.; Wang, P.Y.; Xue, X.; Shan, C.X.; Li, W.H.; Wang, K.; Li, J.H. Seismic performance of precast tubular web reduced beam section connection. *Structures* **2022**, *43*, 1259–1274. [CrossRef]

34. *GB/T 50081-2019*; Standard for Test Methods of Concrete Physical and Mechanical Properties. National Standards of the People's Republic of China; China Building Industry Press: Beijing, China, 2019. (In Chinese)

35. *GB/T 2975-2018*; Steel and Steel Products-Location and Preparation of Samples and Test Pieces for Mechanical Testing. National Standards of the People's Republic of China; Standards Press of China: Beijing, China, 2018. (In Chinese)

36. *GB/T 2281-2021*; Metallic Materials-Tensile Testing-Part 1: Method of Test at Room Temperature. National Standards of the People's Republic of China; Standards Press of China: Bejing, China, 2010. (In Chinese)

37. *JGJ/T 101-2015*; Specification for Seismic Test of Buildings. Industry Standards of the People's Republic of China; China Architecture & Building Press: Beijing, China, 2015. (In Chinese)

38. Wu, K.; Xu, C.; Cao, P.Z.; Lin, S.Q.; Chen, F. Experimental study on the flexural behavior of profile steel-steel fiber reinforced concrete composite beams. *China Civ. Eng. J.* **2019**, *52*, 41–52. (In Chinese)

39. Guo, Z.H.; Shi, X.D. *Reinforced Concrete Theory and Analyse*; Tsinghua University Press: Beijing, China, 2003. (In Chinese)

40. Wang, K.; Wang, Y.H.; Zhou, X.H.; Su, H.; Tan, J.K.; Kong, W.B.; Peng, T. Lateral behaviour and failure modes of buckling-restrained beam-only-connected steel plate shear walls. *Eng. Fail. Anal.* **2022**, *142*, 106833. [CrossRef]

41. Zhang, A.L.; Guo, Z.P.; Liu, X.C. Seismic performance of Z-type cantilever beam splices of column–tree connection. *J. Constr. Steel Res.* **2017**, *133*, 97–111. [CrossRef]

42. *JGJ 82-2011*; Technical Specification for High Strength Bolt Connections of Steel Structures. Industry Standards of the People's Republic of China; China Architecture & Building Press: Beijing, China, 2011. (In Chinese)